

NEUROSCIENCE

Mapping microstructural gradients of the human striatum in normal aging and Parkinson's disease

Elior Drori*, Shai Berman, Aviv A. Mezer

Mapping structural spatial change (i.e., gradients) in the striatum is essential for understanding the function of the basal ganglia in both health and disease. We developed a method to identify and quantify gradients of microstructure in the single human brain in vivo. We found spatial gradients in the putamen and caudate nucleus of the striatum that were robust across individuals, clinical conditions, and datasets. By exploiting multiparametric quantitative MRI, we found distinct, spatially dependent, aging-related alterations in water content and iron concentration. Furthermore, we found cortico-striatal microstructural covariation, showing relations between striatal structural gradients and cortical hierarchy. In Parkinson's disease (PD) patients, we found abnormal gradients in the putamen, revealing changes in the posterior putamen that explain patients' dopaminergic loss and motor dysfunction. Our work provides a noninvasive approach for studying the spatially varying, structure-function relationship in the striatum in vivo, in normal aging and PD.

INTRODUCTION

The striatum, consisting of the caudate nucleus and the putamen, is a major input structure of the basal ganglia, playing a crucial role in motor and cognitive aspects of goal-directed behavior (1). Changes in striatal tissue and interhemispheric asymmetries are associated with motor and cognitive dysfunctions that take place in normal aging (2) and in neurodegenerative disorders such as Parkinson's disease (PD), dystonia, and Huntington's disease (1, 3). The function of the striatum is tightly related to its cellular and biochemical properties: Histochemical studies highlight the distinct neurochemical compartments of the striatal tissue (i.e., striosomes and matrix), which differ in dopaminergic and cholinergic expression and change in distribution and chemical properties along the anatomical axes of the striatum (4–6). These compartments are thought to constitute an organizational feature of striatal connectivity (6–8). The connectivity of the striatum has been linked to the hierarchal organization of the cortex, with gradients of sensorimotor, associative, and limbic domains along the anterior-posterior (i.e., rostral-caudal) and ventromedial-dorsolateral axes (9, 10). Accordingly, electrophysiology and functional magnetic resonance imaging (fMRI) studies have provided evidence for functional and cognitive gradients in the striatum (11–14).

Changes in the striatum's biological spatial variation (i.e., gradients; we use these terms interchangeably) are notably apparent in PD, mainly along the anterior-posterior axis, which emphasizes acute degeneration in posterior parts of the putamen (15–19). This degeneration is characterized by the depletion of dopaminergic innervation to the striatum, due to the patients' loss of dopaminergic neurons in the substantia nigra pars compacta (1). Positron emission tomography (PET) and single-photon emission computed tomography (SPECT) studies in PD patients demonstrate the decrease of dopamine intake in the striatum (20–23). Striatal deterioration, in turn, affects motor function, leading to a range of movement impairments (1, 24). Hence, gradients in the cellular and neurochemical content level (i.e., the microenvironment) of the striatum are a key feature in understanding the striatum's dysfunction in PD.

Microstructural gradients of the striatum are studied mainly using invasive animal research and human postmortem analyses. In living humans, MRI is the primary noninvasive tool for structural research of the brain. Developments in quantitative MRI (qMRI) provide parametric mappings of biophysical tissue properties, such as the longitudinal relaxation rate R_1 , which is sensitive to a variety of biological sources in the microenvironment of the tissue, including myelin, water content, and iron concentration. Therefore, qMRI has been proposed to provide “in vivo histology” of the human brain (25). We hypothesized that incorporating a spatial approach in qMRI methods to map the heterogeneous microstructural properties of subcortical regions, and specifically the striatum, would have important effects for our understanding of aging and PD in vivo.

Here, we present an in vivo method to quantify microstructural gradients in the caudate and putamen in normal aging and PD. Our innovative approach allows the measurement of spatial variation in microstructure along the main axes of the striatum. Using this approach, we characterize striatal gradients that are related to multiple biological sources, in healthy younger and older adults. Next, to detect PD-related microstructural changes, we generalize our results to widely available clinical datasets. We investigate how changes in striatal gradients are related to PD motor symptomatology, as well as to striatal dopamine loss in individual patients. Last, our analysis expands to the relationship between the striatum and the cerebral cortex, identifying a gradient of cortico-striatal microstructure networks, that shows dependency between striatal position and the cortical circuit hierarchical organization (9, 13).

RESULTS

Microstructural gradients in the striatum

Previous studies have identified spatial gradients in the microenvironment along the axes of the striatum ex vivo (4–6). To assess spatial variability in humans in vivo, we developed an automatic tool to express the main axes of the striatum on the single-subject level (Fig. 1A). Our tool uses a region-of-interest (ROI) mask and performs singular value decomposition (SVD) on the voxel coordinates to find the main orthogonal axes of a given region. Voxels are then divided into seven equally spaced segments along each of the axes (see section S1), and the median value of a qMRI parameter

Copyright © 2022
The Authors, some
rights reserved;
exclusive licensee
American Association
for the Advancement
of Science. No claim to
original U.S. Government
Works. Distributed
under a Creative
Commons Attribution
NonCommercial
License 4.0 (CC BY-NC).

The Edmond and Lily Safra Center for Brain Sciences, The Hebrew University of Jerusalem, Jerusalem, Israel.

*Corresponding author. Email: elior.drori@mail.huji.ac.il

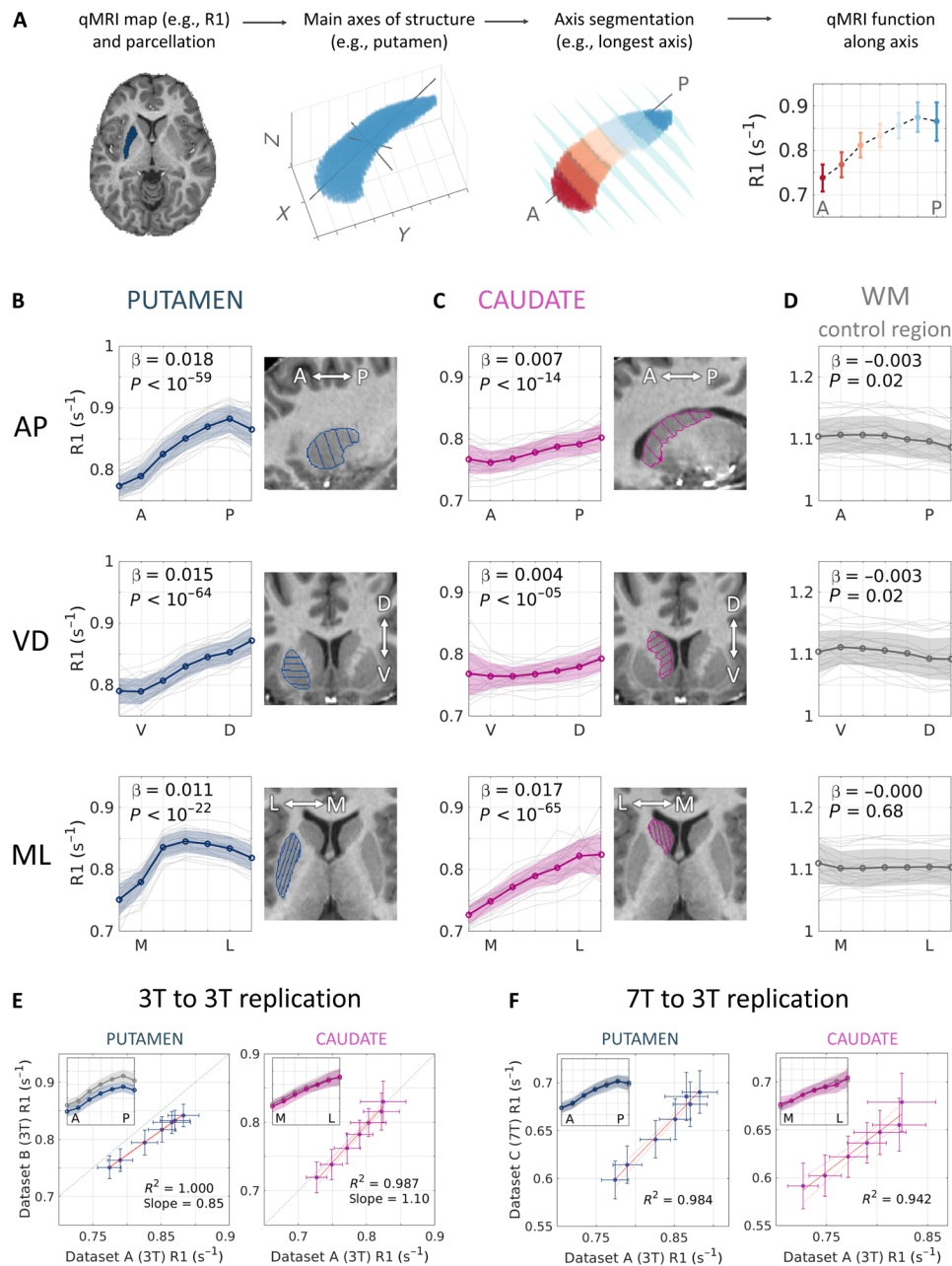


Fig. 1. Microstructural gradients in the striatum revealed in vivo. (A) Automatic computation of the putamen’s AP axis in a single subject and calculation of a microstructural gradient along it. (B and C) R1 gradients along three axes of the left putamen (B) and caudate (C) in 23 young adults (dataset A). The typical spatial change between segments is represented by the fixed effect β , estimated using a mixed-effects model for each axis. The sign of β denotes a positive or negative gradient, i.e., an increase or decrease in R1 (s^{-1}) along the axis. (In subsequent analyses, cases of a nonlinear change along the axis are approximated using two linear models. See Methods and table S1.) P values are FDR-corrected. (D) The R1 functions along axes of a control white matter (WM) region show almost no change, ruling out image bias as an explanation for the measured striatum gradients. (E and F) Replications in two independent datasets (datasets B and C) in 3T (E) and 7T (F). The agreement between datasets is shown in each panel using linear regression between the average R1 functions along the putamen AP axis and along the caudate ML axis. Insets: R1 spatial functions from dataset A (gray) and dataset B or C (color). Data in (F) are z-scored since different strength fields yield different R1 ranges. Shaded areas and error bars represent ± 1 SD.

(e.g., quantitative R1) is computed for each segment, yielding a quantitative function along each axis (see Methods). In Fig. 1 (B and C), we show that in the putamen and caudate, the three main axes roughly correspond to the ROI’s anterior-to-posterior (AP), ventral-to-dorsal (VD), and medial-to-lateral (ML) axes (see section S2 for a detailed quantification).

We found spatial gradients of R1 along the putamen and caudate of healthy, young adult subjects (dataset A: $N = 23$, aged 27 ± 2 years; Fig. 1, B and C). Using mixed-effects linear models (see Methods), we found that these gradients carry significant change along the main axes of the striatal structures, with the most substantial change, expressed as positive gradients (i.e., increases in R1 values), along the

putamen's AP axis and the caudate's ML axis (Fig. 1, B and C; shown for the left striatum). To rule out potential confounds of the measured variability (e.g., MRI field inhomogeneities), we tested for spatial changes in a nearby frontal white matter region of a similar shape and found little to no change along the three axes of this control region (Fig. 1D; see also section S3 and fig. S3). The results were replicated on two independent datasets acquired in different scanners and at different field strength (datasets B and C, corresponding to Fig. 1, C and D, respectively; see also section S4 and figs. S4 to S6). Hence, quantitative R1 mappings reveal reproducible spatial gradients of microstructure in the human striatum.

Aging-related, spatially dependent changes and asymmetry in the striatum

Normal aging is often associated with motor decline and therefore has been proposed to involve striatal changes (2, 26, 27). To investigate aging-related spatial changes in the striatum, we performed three independent cross-sectional studies on three datasets (A, B, and C), each consisting of younger adults and older adults, with a total of $N = 138$ healthy subjects ($N = 41$, $N = 31$, and $N = 67$, respectively). Thus, datasets B and C allow the testing of the robustness of our findings across different MRI scanners and magnetic fields.

First, similarly to younger adults (Fig. 1), older adults also showed robust R1 gradients in the striatum (Fig. 2A). Moreover, we found spatially dependent, aging-related effects (see table S1). In the putamen, we found an interaction effect of age group and position along the VD axis [$P < 0.05$, false discovery rate (FDR)-corrected], demonstrating an aging-related change in the microstructural gradient of the putamen. This result was replicated in dataset B, where we found that this aging-related change also interacted with the hemisphere ($P < 0.05$).

Interhemispheric asymmetries in the volume of the striatum were previously reported as a correlate of aging (26). However, it remains unknown whether aging involves asymmetric changes in striatal microstructural properties. Therefore, we tested for asymmetries in the R1 gradients along the left and right putamen and caudate. While the mean R1 gradients were largely similar for the left and right putamen, for the left and right caudate we found clear, spatially dependent asymmetries, in both younger and older adults (Fig. 2A). In particular, in the left caudate we observed linear gradients along the AP and ML axes, while in the right caudate we observed that the spatial changes followed an inverted U-shape. Accordingly, after accounting for these nonlinearities using a linear approximation (see Methods and section S5), we found interaction effects of hemisphere and position along the AP and ML axes, indicating significant, spatially dependent asymmetries between the left and right caudate ($P < 10^{-22}$). This result was replicated in datasets B and C (table S1). Furthermore, we found an interaction effect of age, hemisphere, and position along the caudate's AP axis ($P < 10^{-5}$), indicating an aging-related increase in the interhemispheric R1 asymmetry. We replicated this effect in dataset B (but not in dataset C; see section S4 for possible interpretations). In a follow-up investigation, we quantified the within-subject asymmetry as the left-minus-right difference (see Methods) and found significant increases in asymmetry in anterior and posterior segments of older adults ($P < 10^{-4}$; Fig. 2, B and C).

These analyses use spatial functions along each region, but we also sought to verify that the information uncovered by our method would not be revealed by looking at the whole region. To do so, we tested for whole-ROI asymmetries in R1 median value and did not

find a difference in caudate asymmetry between age groups (two-sample t test, $t_{38} = 0.5$, $P = 0.6$). This highlights the importance of spatial information for examining aging-related changes.

Biophysical sources of striatal gradients and aging-dependent changes

To investigate the biophysical sources of spatial and aging-related changes in the striatum, we examined the spatial variability of two additional qMRI parameters: $R2^*$, which has been linked to iron concentration (28), and the macromolecular tissue volume (MTV) (29), which is used as an estimator of nonwater content. For each of these parameters, we found distinct spatial functions along the axes of the striatum (Fig. 3, dataset A, excluding five subjects with no $R2^*$ mapping, and figs. S8 to S10).

To estimate the spatial and aging-related changes in each parameter, we used mixed model designs. We found that $R2^*$ increases linearly along the AP axis of the putamen (Fig. 3B and table S2) and decreases linearly along the VD axis of the caudate (fig. S8). Moreover, we found nonlinear, inverted U-shaped $R2^*$ profiles along the VD axis of the putamen and the ML axis of the caudate. These effects interacted with the age group, suggesting an increase in iron spatial variability in older adults (see section S5 for more details on the estimation of nonlinear effects).

In addition, we detected age-group main effects in both $R2^*$ and MTV, however, in opposite directions: Compared to younger subjects, in the caudate and putamen of older subjects, we found increased $R2^*$ but decreased MTV (table S3). Together, these two results suggest higher iron levels and greater tissue loss as a function of aging (Fig. 3, B and C).

To further investigate the contributions of tissue density and iron to the R1 gradients in the striatum, we compared the spatial profiles of MTV and $R2^*$ to those of R1 (see section S8 and figs. S11 to S13). Notably, we found that the spatial change of MTV, as well as the coefficients of the statistical models using MTV, was positively correlated with those of R1. $R2^*$, on the other hand, was less correlated with R1. However, positive correlations between $R2^*$ and R1 were evident along the putamen AP axis and right caudate ML axis. In addition, $R2^*$ and R1 (but not MTV) showed aging-related changes in the putamen VD axis, suggesting iron changes in this axis. This may suggest that the R1 gradients in the striatum not only reflect, to a high degree, variability in tissue density but also are likely to contain iron contributions. Together, our results suggest that aging of the striatum involves local changes in tissue atrophy and iron content. These changes may have opposite effects on the measured R1, which is known to increase with iron and decrease with tissue loss (25, 30). It should be noted, however, that different qMRI measurements show different levels of noise (31). We found that the coefficient of variation (CV) between individual subjects' gradients was higher in MTV and $R2^*$ than in R1 ($P < 10^{-7}$; section S8 and fig. S14). In addition, we found that the CV was higher in older adults compared to younger adults, with the greatest difference in $R2^*$ ($P < 10^{-14}$). Therefore, spatially dependent contributions of tissue density and iron to R1 may not always be expressed as statistically significant effects in MTV or $R2^*$.

Microstructural gradients in PD patients are associated with dopaminergic loss and motor signs

Ex vivo studies have shown that striatal gradient abnormalities are related to PD etiology (15–18). To test whether local changes in the

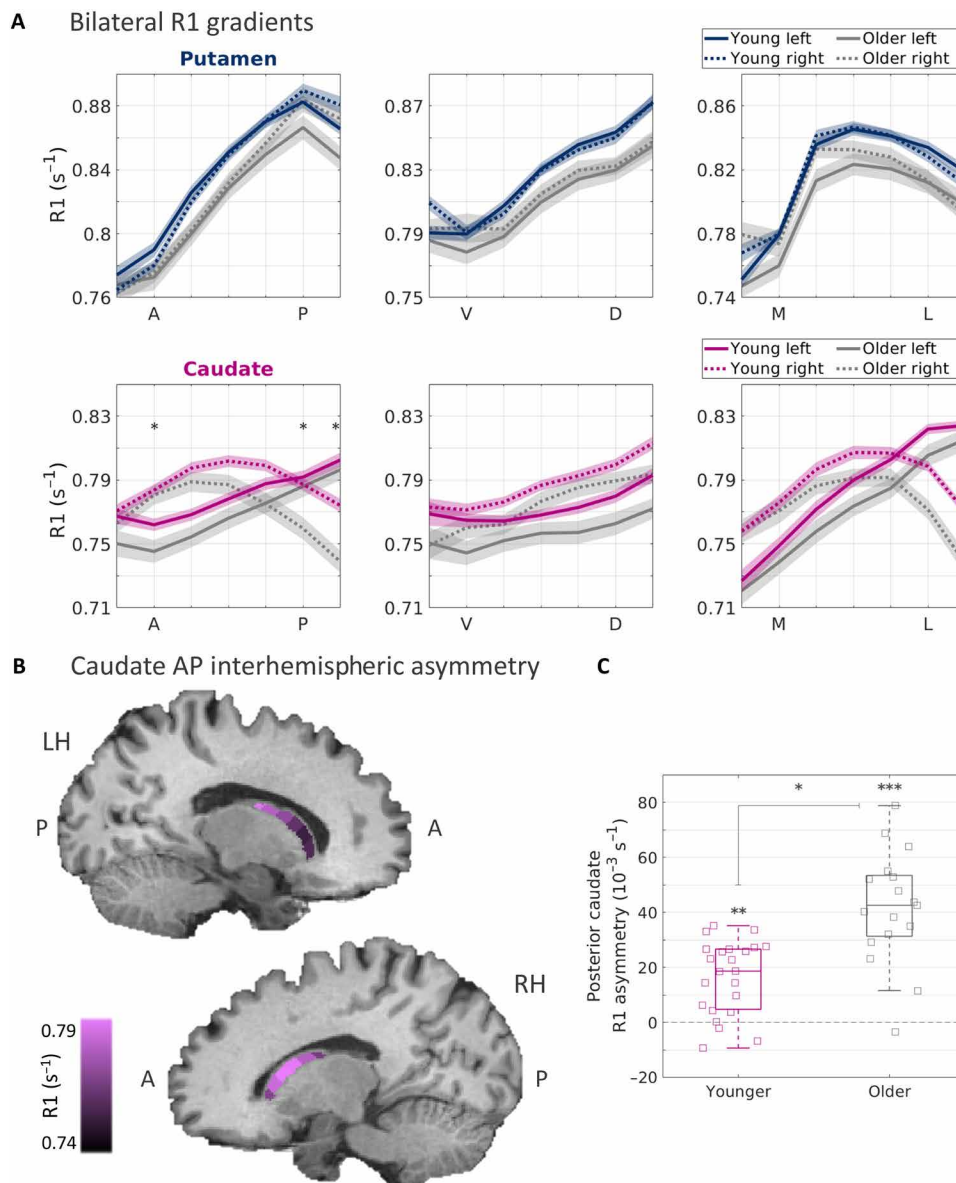


Fig. 2. Striatal R1 gradients reveal aging-related changes. (A) R1 functions along the main axes of the left and right putamen (blue) and caudate (pink), averaged across 23 younger adults and 17 older adults (gray) from dataset A. Shaded areas represent ± 1 SEM. The interhemispheric asymmetry along the AP axis is increased in the older group, as reflected by a three-way interaction effect of age group, hemisphere, and position ($P < 0.001$; see table S1). Asterisks represent segments along the AP axis where the interhemispheric difference was significantly higher in the older group, as shown in (C). (B) Visualization of the mean R1 gradients along the AP axis of the left and right caudate of the older group, overlaid on a T1-weighted image of a sample older adult. (C) Interhemispheric asymmetry is quantified for the posterior segments of the caudate AP axis (averaged across the two most posterior segments). Asymmetry is expressed as the within-subject, left-minus-right difference in R1 values. In each boxplot, the midline and edges represent the median and the 25th to 75th percentiles, respectively. $*P < 10^{-4}$, $**P < 10^{-5}$, and $***P < 10^{-6}$. All P values are FDR-corrected.

striatum can be detected in PD patients in vivo, we analyzed structural MRI data of 99 early-stage de novo PD subjects and 46 healthy controls matched for age ($t = 0.03$, $P = 0.98$) and sex (Pearson's $\chi^2 = 0.3$, $P = 0.58$) from the Parkinson's Progression Marker Initiative (PPMI; demographics and PD characteristics are shown in Table 1).

Since quantitative R1 maps are often not available in clinical settings, we generated semiquantitative maps by dividing T1-weighted images by T2-weighted images (T1w/T2w). T1w/T2w has a contrast similar to R1 and is clean of shared coil biases, and therefore, although it does not have physical units, it is widely used as a semiquantitative

measurement for microstructure in the cortex (32–35). In the striatum, we found that T1w/T2w gradients are similar to those which we identified using R1 [Fig. 4F and fig. S15, PPMI dataset; see fig. S16 for replication with an independent dataset from the Human Connectome Project (HCP) (36)]. This result suggests that our spatial analysis in the striatum can be generalized to other clinical and nonclinical datasets.

Next, we compared the T1w/T2w gradients of PD patients and healthy controls. In all axes of the caudate, T1w/T2w gradients did not separate PD patients from healthy controls; however, in the AP

axis of the putamen, we observed a divergence between the groups. Specifically, mean T1w/T2w values in the posterior segments of the putamen were lower in PD (Fig. 4A and fig. S17). A mixed-effects model revealed a significant interaction between the position along the AP axis of the putamen and the patient group, suggesting a moderate but statistically significant decrease in T1w/T2w values in the posterior putamen in PD ($P_{\text{uncorrected}} = 0.003$; $P_{\text{FDR}} < 0.05$; see table S4). The CV did not differ between PD patients and healthy controls ($P = 0.3$). This result is in agreement with human PD studies and nonhuman models of the disease, which consistently

find PD-related differences in the posterior parts of the putamen (15–17, 37).

Since PD-related changes typically manifest asymmetrically (19), we calculated the interhemispheric T1w/T2w asymmetry in the posterior putamen (see Methods) and tested whether PD patients show asymmetry properties that differ from healthy controls. In the posterior part of the putamen, we found spatially dependent, marginally significant differences between the groups in the asymmetry mean (segment 6, uncorrected $P < 0.05$) and variance (segment 5, Bartlett's test, uncorrected $P < 0.05$).

We then sought to understand how the group differences we found in the posterior putamen of PD patients and healthy controls are associated with disease properties on the single subject level. We tested the linear correlations between the asymmetry of T1w/T2w in the posterior putamen (averaged across the three most posterior segments) and the asymmetry in either dopaminergic loss in the putamen or in parkinsonian motor signs. First, we hypothesized that in the posterior putamen, lower T1w/T2w in one hemisphere relative to the other would be associated with lower dopamine levels in that same hemisphere. We found a positive correlation between the T1w/T2w asymmetry in the posterior putamen and the SPECT-derived dopamine transporter binding ratio (DaT SBR) asymmetry in the putamen ($R^2 = 0.25$, $P < 10^{-7}$; Fig. 4B). Namely, microstructural deficit in the posterior putamen, detected with MRI, follows a laterality pattern that is associated with disease-related dopamine loss, quantified by SPECT.

Second, we hypothesized that T1w/T2w asymmetry would be associated with contralateral asymmetry in parkinsonian motor signs, assessed through the MDS Unified Parkinson's Disease Rating Scale part III (MDS-UPDRS III). We identified a correlation between the microstructural asymmetry and the motor asymmetry such that a

Table 1. Demographics and clinical characteristics of PD patients and healthy controls. HC, healthy controls; H&Y, Hoehn and Yahr scale of PD progression (1 and 2 are both referred to as early stage); MDS-UPDRS III, MDS Unified Parkinson's Disease Rating Scale part III, assessment of motor dysfunction; OFF, patients were evaluated off all antiparkinsonian medication; MoCA, Montreal Cognitive Assessment. For further details, see Methods.

Variable	PD (N = 99)	HC (N = 46)
Age, years	65 ± 6 (range, 55–76)	65 ± 6 (range, 55–76)
Sex, female, N (%)	N = 32 (32.2%)	N = 17 (37%)
H&Y scale, stage 1, N (%)	N = 40 (40.4%)	N = 1 (2%)
H&Y scale, stage 2, N (%)	N = 59 (59.6%)	N = 0 (0%)
MDS-UPDRS III (OFF), score	21.3 ± 9.4 (range, 6–43)	0.9 ± 1.9 (range, 0–11)
MoCA, score	27.4 ± 2.2 (range, 20–30)	27.2 ± 1.9 (range, 23–30)

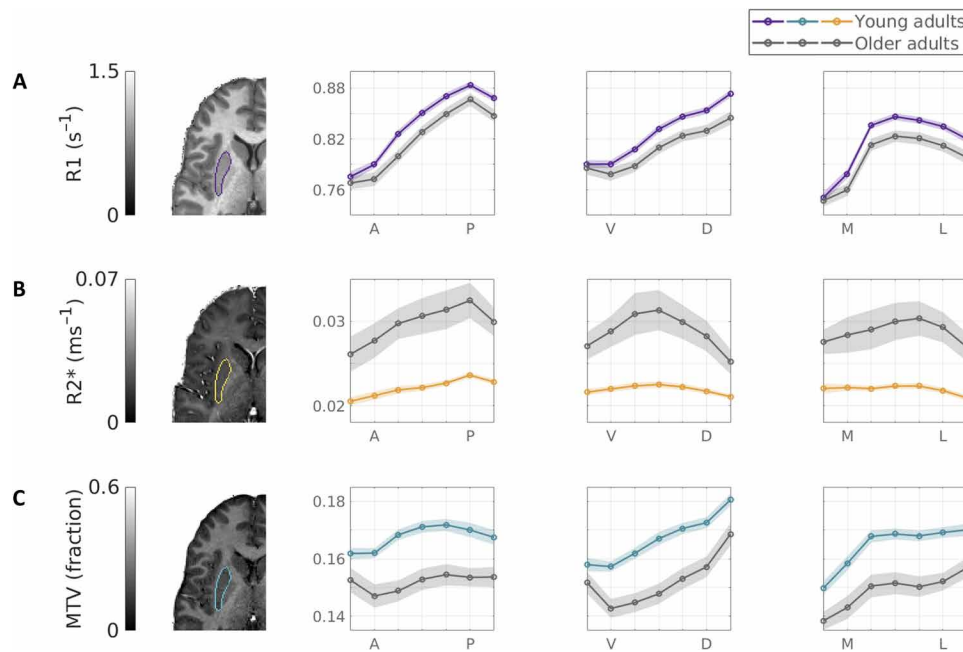


Fig. 3. Multiparametric aging-related gradient change along the main striatal axes. Spatial qMRI functions along the three main axes of the left putamen in younger adults ($N = 17$; color) and older adults ($N = 16$; gray) reveal distinct profiles of change in different biophysical sources. While the tissue longitudinal relaxation rate R1 (A) shows the most significant spatial effects, the iron content correlate R2* (B) shows significant nonlinear spatial change and substantial aging-related increases, and the MTV, or nonwater fraction (C), shows significant decreases in aging. Shaded area is ± 1 SEM.

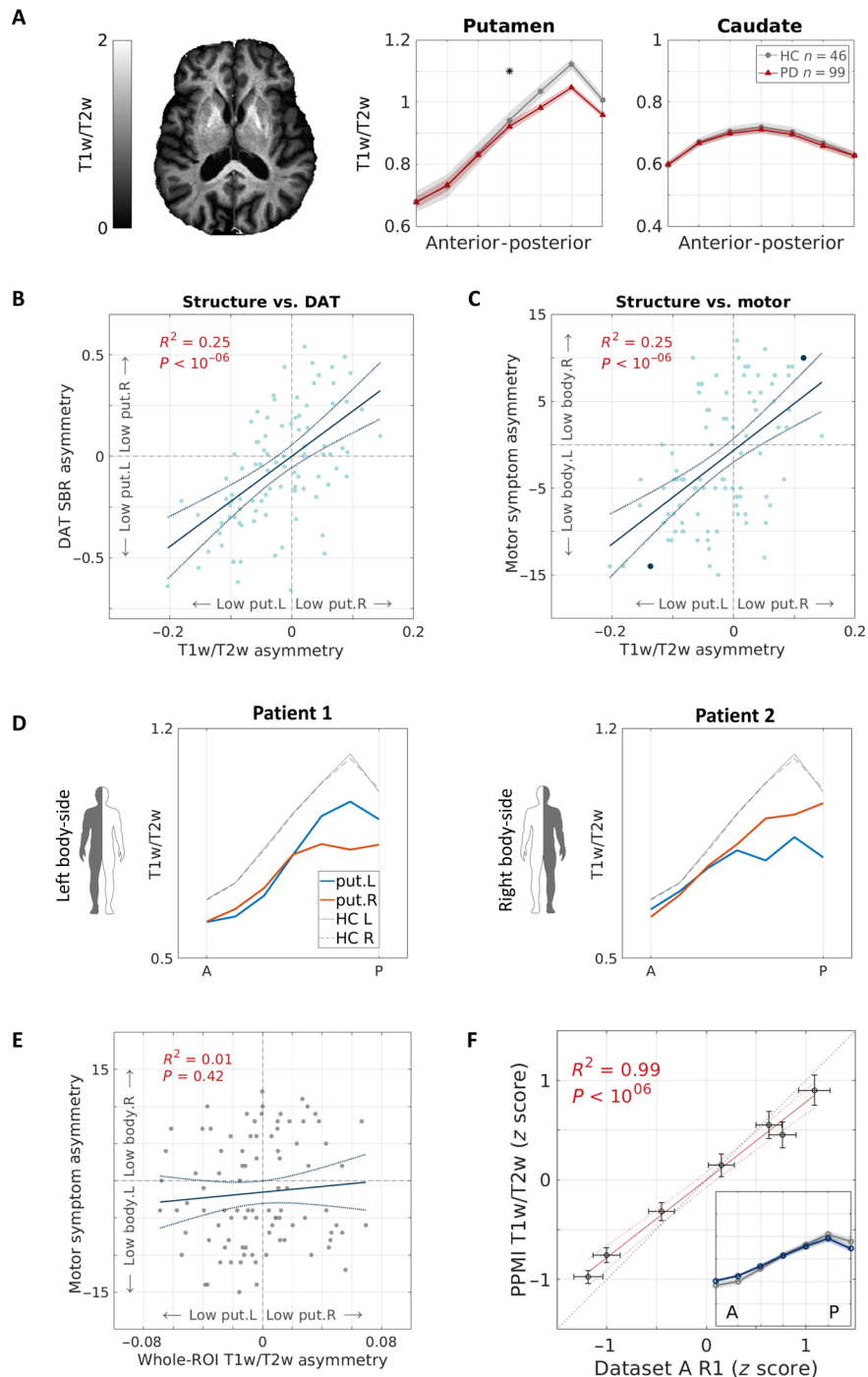


Fig. 4. Putamen gradients reveal microstructure decreases in PD, associated with dopaminergic and motor deficits. (A) T1w/T2w spatial functions are shown for older PD patients ($N=99$) and matched healthy controls ($N=46$) in the AP axes of the putamen and caudate (averaged across hemispheres). The gradient significantly differs between groups, showing a decrease in posterior subregions in PD (linear mixed-effects model, $P_{FDR} < 0.05$). The image shows a representative T1w/T2w axial slice of a PD patient, generated using the PPMI data. (B and C) Microstructural asymmetry in the posterior putamen of PD patients is positively correlated with (B) ipsilateral asymmetry in dopamine transporter binding ratio in the putamen, quantified by DaTSCAN SPECT, and (C) contralateral body-side motor signs. Solid and dashed lines represent the linear fit and 95% confidence interval, respectively. Highlighted in blue are two subjects shown in (D). (D) Individual putamen AP gradients of two PD patients who exhibit motor sign dominance in the left body side (patient 1) and the right body side (patient 2). Both patients show an asymmetric decrease in the posterior putamen that is associated contralaterally to the body side more affected by motor signs. (E) In contrast with our spatial approach, whole-putamen T1w/T2w L-R asymmetry did not show a meaningful correlation with motor asymmetry. $R^2 = 0.01$, $P = 0.42$. (F) Semiquantitative T1w/T2w and quantitative R1 gradients along the AP axis of the putamen show high similarity. Data points represent the seven segments along the putamen's AP axis. We plotted the z-scored, quantitative data of older healthy adults (dataset A, x axis) against the z-scored, semiquantitative data of healthy controls (PPMI data, y axis). Inset: z-scored T1w/T2w gradient (color) and z-scored R1 gradient (gray). Shaded area = ± 1 SEM. put, putamen; HC, healthy controls; L, left; R, right.

lower T1w/T2w in the posterior putamen of one hemisphere was associated with higher motor laterality to the contralateral side of the body ($R^2 = 0.25$, $P < 10^{-7}$; Fig. 4, C and D). Notably, the correlations of microstructural asymmetry with dopaminergic and motor asymmetries were not found for healthy controls ($R^2 < 0.04$, $P > 0.12$) and were not affected by patient's age or sex (see section S10 and fig. S18). Furthermore, we did not find an association between T1w/T2w and the absolute score of motor sign severity (defined as the global MDS-UPDRS III score).

In contrast with our gradient analysis, coarse mean statistics such as the whole-ROI T1w/T2w median value (Fig. 4E) or whole-ROI volume did not reveal relation to motor asymmetry ($R^2 < 0.01$, $P > 0.4$). Furthermore, volumetric asymmetry in the posterior part of the putamen did not show such a correlation, either ($R^2 = 0.02$, $P = 0.16$). Hence, T1w/T2w gradients can uncover spatial information in the microstructure of the striatum that is associated with both PD's abnormal brain changes (i.e., dopamine loss) and symptoms (i.e., motor deficiencies).

Last, we tested for the relationship between T1w/T2w gradient asymmetry and cognitive function, assessed through the Montreal Cognitive Assessment (MoCA) and additional tests (see section S11 and fig. S19), and found no significant correlations. While previous studies reported mixed results regarding association between PD lateralization and cognitive deficits (38, 39), we note that in our study the cognitive state of most our PPMI subjects was within the normal range (see Table 1 and Methods).

A gradient of cortico-striatal covariation

The relationship between structure and function in the striatum, in health and disease, is likely to be mediated by the striatum's relationship to cortical hierarchy (12, 40, 41). Neural tracing and fMRI studies found connectivity and functional correspondence between striatal subregions and the cortex (9, 11). We hypothesized that such connectivity gradients would be reflected in the similarity of microstructural properties between striatal and cortical subregions. Specifically, we performed a structural covariance analysis (see Methods) and tested whether the covariation profiles between the striatum and the cortex change as a function of position along the striatum. We used the semiquantitative T1w/T2w values across a large cohort of healthy, young adult subjects from the HCP ($N = 1067$, aged 29 ± 4 years, 606 female) (36). We identified a gradient of cortico-striatal covariation along the AP axis of the striatum (Fig. 5A). While covariation patterns of posterior regions of the striatum showed little differentiation between cortical areas, anterior regions of the caudate and putamen showed a clear separation between anterior and posterior cortical areas. Specifically, anterior segments of the striatum showed higher positive covariation with frontal and limbic cortices, and negative covariation with more parietal and occipital sensorimotor cortices. This distinction was attenuated gradually toward posterior segments (Fig. 5, B and C, and fig. S20). While the biological meaning of positive and negative structural covariation remains an open question (42, 43), this result provides evidence for a structural gradient of differential cortico-striatal association along the AP axis of the striatum.

DISCUSSION

Our results provide a new approach for the quantification of microstructural variation in the human striatum in vivo, both within and

between subjects. By developing a structural analysis tool, we found that qMRI parameters reveal microstructural gradients along the main axes of the putamen and caudate in healthy young adults. We further showed that these gradients change in normal aging. In generalizing our analysis to clinical MRI, we uncovered an in vivo microstructural correlate of PD, which is associated with both dopamine loss and disease-related motor function impairments. We further demonstrated cortico-striatal relations by showing a structural dependency between striatal position and cortical hierarchy.

Our fundamental finding is the in vivo detection of microstructural gradients in the healthy striatum. This finding is consistent with prior animal and postmortem works that found molecular and connectivity gradients in the healthy striatum, using histochemical staining and neural tracing techniques (4, 9). It was proposed that developmental gradients of cell migration and signaling in the striatum are what give rise to the healthy neurochemical and connectivity gradients (44). In vivo human research also found gradients of connectivity and function, along the AP, VD, and ML axes of the striatum, using diffusion MRI tractography, resting-state fMRI, and task-based fMRI (10–14, 45, 46). For example, Marquand *et al.* (45) found resting-state fMRI topographies that showed a distinction between the putamen and caudate, as well as a common gradient along the AP, VD, and ML axes. O'Rawe *et al.* (46) found distinct resting-state fMRI gradients in the putamen and caudate, with a dominant ML component within the caudate. In agreement with those studies, our results show distinct microstructural gradients in the putamen and caudate, as well as common principles. In the putamen, R1 gradients were found most prominently along the AP and VD axes, while in the caudate the ML axis was most prominent.

Our results demonstrate the value of multiparametric qMRI mapping in studying the biophysical sources of striatal variability and structural changes in aging. In the striatum, spatial R1 variation often correlates with the changes in macromolecular tissue density, quantified by MTV. In addition, we identified aging-related reductions in MTV and increases in $R2^*$. Aging had been shown to involve $R2^*$ increases, which are most substantial in the pallidum and the striatum (47) and are correlated with postmortem iron levels in these regions (28, 47). We also found a positive gradient of $R2^*$ along the AP axis of the putamen, which agrees with postmortem measurements (48). It is therefore likely that the unique profile of $R2^*$ changes in our analysis reflects both aging-related increases and spatial variation of iron in the striatum. While we found interaction effects revealing spatially dependent aging changes in R1, the main effects of age on R1 were not statistically significant in our main dataset A. R1 is widely considered as a myelin- and iron-sensitive measurement (49, 50). It is therefore possible that the two competing aging effects (namely, tissue reduction, quantified by MTV, and iron increase, reflected by $R2^*$) sum up to the insignificant main effect of aging-related decrease in R1. Differences between datasets in R1 aging effects may also be the result of different sample sizes (see Methods; for other possible interpretations, see section S4).

Our findings highlight different kinds of microstructural changes in normal aging and PD. In normal aging, we found changes along different axes of the striatum, including asymmetry increases in anterior and posterior segments of the caudate. In contrast, the microstructural change in early-stage PD was specific to posterior segments of the putamen.

To study the PD effects on the striatum's microstructure, we used the semiquantitative contrast of T1w/T2w. T1w and T2w images

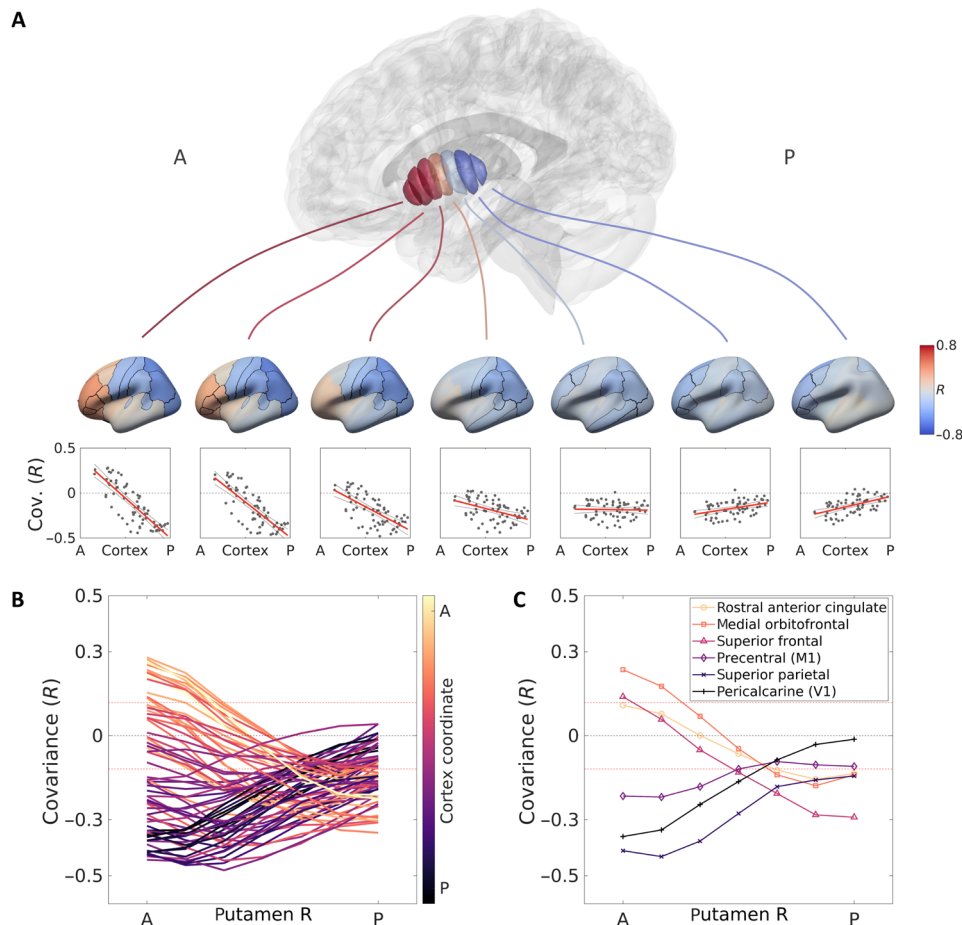


Fig. 5. Microstructural gradient of cortico-striatal covariation shows fronto-limbic to sensorimotor separation. (A) Segments along the putamen's AP axis show distinct profiles of microstructural covariation with cortical regions. Anterior segments of the putamen display differentiative profiles, showing positive covariance with frontal cortical regions and negative covariance with parieto-occipital regions. This differentiation attenuates toward posterior segments of the putamen that show only negative covariance (results are shown for the right putamen). (Similar results are obtained for the left putamen and for the caudate; see fig. S20.) (B) Each of 68 cortical regions (defined by the Desikan-Killiany atlas) is colored with respect to its location on the brain's AP axis (y coordinate of the region's centroid). Profiles of covariation with putamen segments are different for frontal (yellow) and posterior (purple) cortical regions. Red dashed lines indicate bounds of significant covariance (corrected for multiple comparisons). (C) Isolation of example cortical profiles from (B), showing positive covariation of frontal and limbic regions and negative covariation of motor and sensory regions with the anterior putamen, and a gradual change of this trend toward the posterior putamen.

are abundant in clinical and research settings, making our approach widely applicable to existing data. Although the values of T1w/T2w do not have a physical meaning, we have shown that standardized T1w/T2w spatial variation in the striatum is similar to that of quantitative R1 to a large extent. This may suggest that PD-related changes in T1w/T2w reflect general atrophies of the striatal tissue, which may be a consequence of depletions in dopaminergic innervation. Quantitative mapping of PD individuals may shed more light on PD degeneration mechanisms.

Specifically, in PD, we found irregular gradients of T1w/T2w, which show decreases in posterior segments of the putamen. We found that T1w/T2w asymmetry in the posterior putamen was associated ipsilaterally with asymmetric dopamine depletion on the subject level. This result is consistent with human and nonhuman primate studies in PD that identified spatially differential tissue alterations, and specifically inhomogeneous dopaminergic degeneration that is most pronounced in posterior parts of the putamen (15–17). Furthermore, we found that T1w/T2w asymmetry in the putamen was

contralaterally correlated with motor signs' laterality. This finding corroborates previous PET studies that show correlations between the uptake of ^{18}F -l-3,4-dihydroxyphenylalanine (^{18}F -DOPA) in the posterior putamen and the severity of contralateral motor signs (37). The PD patients analyzed in our study were de novo, early-stage patients, with median disease duration of 4 months from diagnosis (see Methods). A previous study showed that motor and dopamine depletion asymmetries were higher in de novo patients and were reduced in a 2-year follow-up evaluation (51). Thus, our study provides a noninvasive imaging correlate for early-stage PD laterality in terms of both dopamine loss and motor function decline.

Using a covariance network analysis, we found a gradient of cortico-striatal structural covariation that corresponds to known connectivity patterns (9, 52). While posterior segments of the striatum do not show differentiation between cortical regions, anterior segments show positive covariations with frontal associative and limbic regions, and negative covariations with sensorimotor parietal and occipital regions. This network analysis is based on the patterns of

structural correlations between brain regions across multiple subjects. Covariance analysis is widely used to study structural and functional networks of the brain, including cortico-cortical (53, 54) and cortico-subcortical (13, 55) networks. Using this approach, recent studies have identified large-scale cortico-cortical gradients that relate to cortical hierarchical organization (53, 54, 56, 57), and Tian *et al.* (13) found resting-state functional gradients of cortico-subcortical networks. To our knowledge, our analysis is the first to identify cortico-striatal structural covariation gradients along the striatum, rather than analyzing the entire putamen or caudate collectively. The underlying neural mechanisms behind structural covariation (and especially the meaning of negative versus positive covariation) are still the subject of active discussion: It has been suggested that structural covariance between regions reflects their involvement in the same functional system, which may manifest through synchronous activation, physical connectivity, or coordinated development (42, 43).

Our findings of cortico-striatal networks strengthen the view of differential involvement of striatal areas in different neural domains. Moreover, our results converge with previous findings of selective connectivity and activity of the anterior striatum. For example, Haber *et al.* (9, 58) showed that projections from prefrontal and limbic cortical regions not only terminate primarily in the anterior striatum but also extend posteriorly. However, motor and premotor projections terminate in the posterior striatum but do not extend to the anterior striatum. In addition, an fMRI study found that while a posterior region of the caudate was engaged during different levels of cognitive processing, anterior regions were involved only in higher-level cognition (11). Our cortico-striatal covariance findings provide further evidence for fronto-limbic versus sensorimotor differentiation in the anterior striatum at the microstructural level.

Both the cortico-striatal covariance and PD results suggest a functional relevance of the putamen AP axis. In the HCP dataset, we found a preferential covariance in the anterior putamen's segments with regard to cortical hierarchy, but for the posterior segments, we found negative or insignificant covariance with all cortical regions. In PD, we found a microstructural reduction posteriorly, which was associated with motor function, but not cognitive function. Taken together, these results suggest that positive covariance in the anterior putamen may reflect higher association with cortical regions involved in cognitive function, which was not affected by the posterior reduction in early-stage PD. Future studies may investigate the implications of PD on cortico-striatal structural covariance directly, using a large PD sample size needed for the analysis.

Our newly developed, automated tool for in vivo microstructural quantification is the first of its kind. Previous studies parcellated the striatum into distinct functional or structural subregions, resulting in atlases that may differ from one another in the number and boundaries of the subregions (13, 59). Our approach is different and complementary to these studies: We do not aim to define distinct subparts but rather provide a compact description for biological gradients, i.e., the spatial change of biophysical properties within the striatum. To date, there are several automated tools for measuring changes in qMRI parameters along white matter tracts and across cortical layers (60–63). Our approach is the first to provide a robust, automatic quantification of qMRI spatial variation along axes of subcortical gray matter structures at the single-subject level. Other studies have developed gradient analyses and found function and connectivity gradients in the striatum. For example, Marquand *et al.* (45) developed a gradient analysis using resting-state fMRI in the

Montreal Neurological Institute (MNI) space and showed cortico-striatal coactivity topographies. This analysis was adapted for use with diffusion MRI tractography data (64). This analysis defines gradients by the eigen decomposition of a graph Laplacian, computed on a parameter matrix of voxel-to-voxel correlations. In contrast, our approach defines the axes first, independently of the parameter, and then samples biophysical parameters along them. Consequently, our method might not follow the axis of largest variance in the parameter.

While this poses a limit on our method, it also has several clear benefits. First, our method allows a comparison across subjects without requiring a voxel-to-voxel correspondence. This eliminates the need to transform the images to a common coordinate frame for a voxel-based analysis (e.g., MNI), a process that involves inevitable information loss (65) and lacks precision for the individual subject level (60, 66). Second, since we define the striatum's axes based on the ROI's coordinate distribution, the identified gradients carry a clear and simple anatomical meaning. Namely, with our method, we are comparing corresponding positions in the ROI across subjects. Furthermore, by computing axes that are independent of the measured parameter, we can compare the spatial change of different biophysical properties (e.g., R1, R2*, and MTV) along the same spatial axes, on both the individual level and the group level. Similar to other gradient analyses, future applications of our tool are not limited to the striatum, as it can be adapted for other subcortical structures such as the pallidum and the brainstem. (For additional analysis and comparison to voxel-based gradients, see sections S12 and S13 and figs. S21 and S22.)

To conclude, we propose a noninvasive quantitative approach to measure microstructural gradients in the human striatum in vivo. Our method provides a unique insight on aging- and disease-related local changes in the striatal tissue. Using different qMRI parameters, we found age-related, spatially dependent changes in the caudate and putamen. Moreover, we found that local alterations in the putamen constitute a signature of PD, which is related to the single-subject dopaminergic loss and motor function decline. Our study elucidates the relations of microstructure variation to biophysical sources on the one hand and to function on the other hand. Future applications should benefit the research and personalized medicine of additional basal ganglia-related degenerative diseases, such as Huntington's disease and dystonia, as well as other disorders that are thought to involve spatial changes in the striatum, such as drug addiction and schizophrenia (3, 52).

METHODS

Datasets

Main 3T dataset (dataset A)

The dataset was collected in a previously published work; for full details, see Filo *et al.* (30). All study procedures were approved by the Helsinki Ethics Committee of Hadassah Hospital, Jerusalem, Israel. A written informed consent was obtained from all participants before the procedure.

Subjects. Measurements were performed on healthy individuals in two age groups: 23 young adults (aged 27 ± 2 years; range, 23 to 31) and 18 older adults (aged 67 ± 6 years; range, 55 to 75). We excluded one older female subject from our analysis due to a detected abnormality in her caudate nucleus.

Data acquisition. Data were collected on a 3T Siemens MAGNETOM Skyra scanner at the Edmond and Lily Safra Center (ELSC) neuroimaging unit at the Hebrew University of Jerusalem. For quantitative R1, R2*,

and MTV mappings, three-dimensional (3D) spoiled gradient echo (SPGR) images were acquired with four different flip angles ($\alpha = 4^\circ, 10^\circ, 20^\circ, \text{ and } 30^\circ$). Each image included five equally spaced echoes, with echo time (TE) of 3.34 to 14.02 ms, except for five young subjects for whom the scan included only one TE (3.34 ms). The repetition time (TR) was 19 ms, and the scan resolution was 1 mm^3 isotropic. For bias estimation, spin-echo inversion recovery images were acquired with echo-planar imaging readout (SEIR-EPI). For these images, sequence parameters were TE = 49 ms, TR = 2920 ms, and inversion time (TI) = 200, 400, 1200, and 2400 ms. Slice thickness was 3 mm, and in-plane resolution was 2 mm^2 . In addition, anatomical T1w images were acquired with either 3D magnetization-prepared rapid gradient echo (MPRAGE) or magnetization-prepared two rapid acquisition gradient echoes (MP2RAGE).

Estimation of qMRI parameters. Whole-brain R1 and MTV maps, as well as field bias maps of excitation (B1+) and receive (B1-) for correction, were computed using mrQ software (<https://github.com/mezera/mrQ>) (29).

For subjects ($N = 36$) scanned with multiple echo SPGR, R2* fitting was done using the MPM toolbox (67). R2* estimates acquired from each of the four SPGR images were averaged for increased signal-to-noise ratio (SNR).

MTV was corrected for R2* residuals using the following equation:

$$\text{MTV}_{\text{corrected}} = 1 - (1 - \text{MTV}) \cdot \exp(\text{TE} \cdot \text{R2}^*)$$

where $\text{MTV}_{\text{corrected}}$ was used throughout our analysis.

Brain segmentation. Subcortical gray matter structures were segmented using FSL's FIRST probabilistic segmentation tool (68). The subject's MPRAGE or MP2RAGE scan was used as a reference image. Images were registered to the MTV space before the segmentation, using rigid-body registration. To avoid partial volume effects, the outer 1-mm shell of each structure was removed. All segmentations were inspected by eye to avoid ROI misclassifications and ensure their quality.

Replication 3T dataset (dataset B)

Subjects and data. Data used for replication in 3T are from a previously published work (69). All data collection procedures were approved by the Stanford University Institutional Review Board, and each participant provided informed consent.

The data were collected on a 3T Discovery 750 MRI system (General Electric) at the Center for Cognitive and Neurobiological Imaging at Stanford University. For R1 mapping, SPGR images were acquired with four different flip angles ($\alpha = 4^\circ, 10^\circ, 20^\circ, \text{ and } 30^\circ$), TR = 14 ms, and TE = 2.4 ms. Scan slice thickness was 1 mm, and the in-plane resolution was 0.94 mm^2 . From these data, we used subjects in two age groups: 15 young adults (aged 25 ± 5.5 years; range, 18 to 32; 10 females) and 16 older adults (aged 70 ± 8 years; range, 58 to 85; 8 females). Estimation of quantitative R1 and brain segmentation were done using the same procedure as in our main dataset.

Replication 7T dataset (dataset C)

Subjects and data. We used the open source AHEAD 7T preprocessed qMRI dataset (<https://doi.org/10.21942/uva.10007840.v1>). The study was approved by the ethical committee of Xuanwu Hospital of Capital Medical University. All participants have provided written informed consent; for full details, see Alkemade *et al.* (70). Data were acquired at the Spinoza Centre for Neuroimaging in Amsterdam, using an MP2RAGE sequence in a Philips Achieva 7T MRI scanner. Image resolution was 0.7 mm^3 isotropic. The data include T1w images

as well as quantitative R1, R2*, and susceptibility mappings (estimation of MTV was not possible for dataset C since it was not acquired using SPGR sequence). The data consist of 105 subjects aged 18 to 80 years. From these data, we chose 67 subjects who fall in one of two age groups: young adults ($N = 42$; range, 18 to 30 years; 27 females) and older adults ($N = 25$; range, 51 to 70 years; 14 females). Subjects' exact ages were not available. Segmentation was done in the same procedure as in our main dataset, using the T1w images as reference.

T1w/T2w dataset (HCP)

Subjects and data. Data were obtained from the publicly released HCP Young Adult dataset, consisting of 1206 healthy young adults (age range, 22 to 37 years) (36). We chose 1113 subjects who had T1w and T2w data of high resolution (0.7 mm^3 isotropic). From these, we excluded 35 subjects who were flagged by the HCP preprocessing pipeline as part of segmentation and surface reconstruction quality control ("Issue code B"; see <https://wiki.humanconnectome.org/pages/viewpage.action?pageId=88901591>). We further excluded 11 additional subjects for whom FSL FIRST failed to produce a proper subcortical segmentation, yielding a total of $N = 1067$ subjects in our analysis. Cortical parcellation was done and provided by the HCP, using FreeSurfer (71) based on the Desikan-Killiany atlas (72). For further information, see www.humanconnectome.org/study/hcp-young-adult/document/1200-subjects-data-release. Subcortical segmentation was done using FSL's FIRST, following the same procedure applied for our main dataset [see the "Main 3T dataset (dataset A)" section] and using the T1w image as a reference.

PD T1w/T2w dataset (PPMI)

Subjects and data. Data used in the preparation of this article were obtained from the PPMI database (www.ppmi-info.org/access-data-specimens/download-data). For up-to-date information on the study, visit www.ppmi-info.org. PPMI—a public-private partnership—is funded by the Michael J. Fox Foundation for Parkinson's Research and funding partners, found at www.ppmi-info.org/about/ppmi/who-we-are/study-sponsors.

For our analysis, we chose 99 older, early-stage, de novo PD patients (aged 65 ± 6 years; range, 55 to 76; 32 female), all of whom were classified to be at the Hoehn and Yahr scale's stage 1 ($N = 40$) or stage 2 ($N = 59$). The median duration of disease between PD diagnosis and imaging was 4 months, with median absolute deviation of 6.6 months. We also chose 46 healthy controls matched for age and sex (aged 65 ± 6 years; range, 55 to 76; 17 female). Both patients and controls underwent the same protocols, including T1w and T2w scans, DaTSCAN, and behavioral assessments.

MRI scanning. MRI data were collected using a 3T SIEMENS Trio scanner. T1w images were acquired using an MPRAGE generalized autocalibrating partially parallel acquisitions (MPRAGE-GRAPPA) sequence, with 1-mm sagittal slice thickness and 1-mm^2 in-plane resolution. T2w images were acquired using a turbo spin echo (TSE) sequence with 3-mm axial slice thickness and 0.94-mm^2 in-plane resolution.

T1w/T2w images. The T1w/T2w ratio provides a semiquantitative contrast since it minimizes the shared bias of the weighted images. To generate T1w/T2w images, we resampled the T2w images to match the T1w images' 1-mm^3 isotropic resolution. Registration, alignment, and resampling of the T2w images to T1w images were performed using software packages from SPM (www.fil.ion.ucl.ac.uk/spm/software/spm12/) and MRtrix3 (www.mrtrix.org/). T1w image intensities were then divided by T2w image intensities voxel-wise. All steps were inspected by eye to ensure image quality. Segmentation

was done in the same procedure as in our main dataset, using the T1w images as a reference.

DaTSCAN. 123I-FP-CIT SPECT imaging was performed on all subjects for assessment of dopamine transporter (DAT) deficit. Radiotracer striatal binding ratio (SBR) was calculated for the putamen and caudate in each hemisphere at the Institute for Neurodegenerative Disorders (IND) at Yale University, New Haven. For further details, see www.ppmi-info.org. We calculated DaT SBR asymmetry per subject as the left putamen SBR minus the right putamen SBR (L-R).

Motor function and asymmetry. Motor signs were assessed through MDS-UPDRS III, off any antiparkinsonian medications. The patients' scores were within the range of 6 to 43, with a mean \pm SD of 21.3 ± 9.4 . For the healthy control subjects, scores were in the range of 0 to 4, except for one subject with score 11 (0.9 ± 1.9). We defined an individual's motor signs asymmetry score as the sum of raw scoring for the left body-side items minus the sum of right body-side items (L-R) such that a greater positive score implies a left-side laterality and a greater negative score implies a right-side laterality.

Cognitive assessments. Subjects were assessed for cognitive deficits through a battery of tests and assessments. In our analysis, we used the scores from the MoCA, Benton Judgement of Line Orientation, Hopkins Verbal Learning Test, Letter-Number Sequencing Test, Symbol Digit Modalities Test, and Semantic Fluency.

MoCA scoring ranges between 0 and 30, where a score of 26 and over is considered cognitively normal. The patients' scores were at the range of 20 to 30, with most patients within normal range (mean \pm SD of 27.4 ± 2.2).

qMRI gradients

We developed an automatic procedure to generate qMRI functions along the main axes of a subcortical structure at the single-subject level. Without needing to rotate the image, this procedure moves from image axes to ROI-based axes and then samples qMRI values as a function of position along them.

Automatic axis computation

Given an ROI mask (or a segmentation file and label), the algorithm computes the SVD of the ROI's voxel 3D image coordinates to find the main three orthogonal axes (i.e., the eigenvectors) of the structure. The SVD algorithm solves for

$$M = U \Sigma V^*$$

where M is an $m \times 3$ matrix of the ROI's m centered image coordinates, Σ is a diagonal matrix with the singular values of M , and U and V are matrices whose columns are the left and right singular vectors of M , respectively (or the orthonormal eigenvectors of MM^* and M^*M , respectively). Therefore, the columns of the 3×3 matrix V define the main orthogonal axes of the ROI, based on its anatomical shape.

Axis segmentation

For each of the three main axes, we segment the ROI with equal spacing. For this purpose, we define the data edges as the two hyperplanes defined by the two extreme data points of the data with respect to the axis and by the axis as a normal to the plane. The data are then segmented by $n - 1$ parallel hyperplanes equally spaced between the two data edges. Voxels are then classified to n segments based on criteria of distance from planes. For our analysis, we chose $n = 7$.

qMRI functions

Given a qMRI map (e.g., R1), a median value is computed for each segment along each axis. This yields three map-based functions of spatial position ("gradients") along the three main axes of the given ROI.

The longest axis of the putamen and caudate is identified as the anterior-posterior axis, based on the most closely matching brain axis, followed by the ventral-dorsal and medial-lateral axes. To determine the directionality of each axis in a consistent way between individuals (i.e., AP and not posterior-to-anterior), we assume an MRI axis convention such that the image's x , y , and z axes increase from left to right, from posterior to anterior and from inferior to superior, respectively ("LPI"). We determine the directionality of the SVD-derived axes as the following: the longest axis decreases with the y coordinate (AP), the middle axis increases with the z coordinate (VD), and the shortest axis increases with the x coordinate in the right hemisphere and decreases with the x coordinate in the left hemisphere (ML). For each axis, spatial functions are then averaged across subjects of the same condition (e.g., age and clinical group) to provide group-averaged functions of spatial change for the ROI. The MATLAB (www.mathworks.com/) implementation of our tool is available for access at <https://github.com/MezerLab/mrGrad>.

Interhemispheric asymmetry

For each striatal segment, we defined interhemispheric asymmetry on the subject level as the left-hemisphere value minus the right-hemisphere value. We used this formulation for quantitative measurements, while for the semiquantitative measurement (i.e., T1w/T2w) we further normalized this difference across subjects by the mean value across hemispheres

$$R1 \text{ asymmetry} = R1_{\text{Left}} - R1_{\text{Right}}$$

$$T1w/T2w \text{ asymmetry} = \frac{T1w/T2w_{\text{Left}} - T1w/T2w_{\text{Right}}}{(T1w/T2w_{\text{Left}} + T1w/T2w_{\text{Right}})/2}$$

With this definition, a negative value reflects higher MRI value in the right hemisphere, and a positive value reflects a higher MRI value in the left hemisphere.

Statistical analysis

Linear mixed-effects statistical models

Statistical inference for spatial, interhemispheric, and either aging- or disease-related effects was performed using linear regression mixed-effects design models. By default, we used one model for each axis of the caudate or putamen. Since we observed that in some axes the spatial qMRI function showed a quadratic shape, we tested different polynomial degrees for each axis of change before the statistical modeling. For axes where we found that a quadratic fit outperformed the linear fit, we performed a linear approximation of the function by breaking it into two approximately linear parts and modeled each part using a linear model (see section S5). In our model, we expressed the position along the axis, the hemisphere (two levels) and the age or clinical group (two levels) as fixed effects, the subject IDs as a random effect, and the MRI value as the response variable. We tested for the main effects of the fixed variables (position, hemisphere, and subject group), as well as all their interactions. In addition, we used sex as a covariate for the age or clinical group in the model, controlling for their interaction. In addition, in the PD analysis, we tested interactions of the age covariate with the clinical group. The

P values were corrected for multiple comparisons using the Benjamini-Hochberg method (73) for FDR.

Additional group-level comparisons

Differences between subject groups in continuous variables (i.e., age, interhemispheric asymmetry, and CV) were tested using two-sample *t* tests for mean difference. Differences in sex were tested using Pearson's chi-square test (χ^2). All tests were conducted with two-tailed α of 0.05, and corrections for multiple comparisons using FDR (unless reported otherwise).

PD-related variable correlations

To test the relationships between the putamen's T1w/T2w structural gradient asymmetry and either dopaminergic loss or motor function asymmetry, we fitted linear regression models. We report adjusted R^2 values, which represent the proportion of variance explained by the structural asymmetry variable. To rule out effects of age and sex, we added these variables as covariates in the regression models to test for main effects and interactions with the predictor variable (see section S10).

Gradient similarity across datasets

To assess the similarity of gradients obtained in different datasets, we used a linear regression model for each gradient. Observations were group-average values in each segment along the gradient, obtained from two datasets. If the comparison was done between different MRI parameters (i.e., quantitative R1 versus T1w/T2w ratio), the variables were *z*-scored first. Therefore, the level of linearity in the models (as represented by R^2) indicates how similar the datasets are with respect to their relative spatial changes along the axes.

Cortico-striatal T1w/T2w covariation

To identify microstructural associations between cortical regions and striatal subregions, we performed a structural covariation analysis across a large cohort of 1067 subjects from the HCP dataset. Within each cortical region, T1w/T2w values were sampled along the mid-thickness surface of the cortical gray matter, and their mean values were calculated using FreeSurfer (74). To account for any subject-specific bias that may exist in the semiquantitative T1w/T2w images, we calculated the *z* score across the brain regions per subject. Last, we calculated correlations across subjects between the standardized values of each segment along the AP axis of either the putamen or caudate, and the standardized values in each of the cortical regions. The significance level (α) was set using the Bonferroni method for multiple comparisons correction, as follows: initial α of 0.05, divided by 1904 comparisons (4 striatal ROIS \times 7 segments \times 64 cortical regions = 2.6×10^{-5}).

SUPPLEMENTARY MATERIALS

Supplementary material for this article is available at <https://science.org/doi/10.1126/sciadv.abm1971>

REFERENCES AND NOTES

1. P. Redgrave, M. Rodriguez, Y. Smith, M. C. Rodriguez-Oroz, S. Lehericy, H. Bergman, Y. Agid, M. R. DeLong, J. A. Obeso, Goal-directed and habitual control in the basal ganglia: Implications for Parkinson's disease. *Nat. Rev. Neurosci.* **11**, 760–772 (2010).
2. W. A. Cass, R. Grondin, A. H. Andersen, Z. Zhang, P. A. Hardy, L. K. Hussey-Andersen, W. S. Rayens, G. A. Gerhardt, D. M. Gash, Iron accumulation in the striatum predicts aging-related decline in motor function in rhesus monkeys. *Neurobiol. Aging* **28**, 258–271 (2007).
3. J. R. Crittenden, A. M. Graybiel, Basal ganglia disorders associated with imbalances in the striatal striosome and matrix compartments. *Front. Neuroanat.* **5**, 59 (2011).
4. A. M. Graybiel, C. W. Ragsdale, Histochemically distinct compartments in the striatum of human, monkeys, and cat demonstrated by acetylthiocholinesterase staining. *Proc. Natl. Acad. Sci. U.S.A.* **75**, 5723–5726 (1978).
5. L. Prensa, J. M. Giménez-Amaya, A. Parent, Chemical heterogeneity of the striosomal compartment in the human striatum. *J. Comp. Neurol.* **413**, 603–618 (1999).
6. J. G. Johnston, C. R. Gerfen, S. N. Haber, D. van der Kooy, Mechanisms of striatal pattern formation: Conservation of mammalian compartmentalization. *Dev. Brain Res.* **57**, 93–102 (1990).
7. F. Eblen, A. M. Graybiel, Highly restricted origin of prefrontal cortical inputs to striosomes in the macaque monkey. *J. Neurosci.* **15**, 5999–6013 (1995).
8. M. M. McGregor, G. L. McKinsey, A. E. Girasole, C. J. Bair-Marshall, J. L. R. Rubenstein, A. B. Nelson, Functionally distinct connectivity of developmentally targeted striosome neurons. *Cell Rep.* **29**, 1419–1428.e5 (2019).
9. S. N. Haber, Corticostriatal circuitry. *Dialogues Clin. Neurosci.* **18**, 7–21 (2016).
10. B. Draganski, F. Kherif, S. Kloppel, P. A. Cook, D. C. Alexander, G. J. M. Parker, R. Deichmann, J. Ashburner, R. S. J. Frackowiak, Evidence for segregated and integrative connectivity patterns in the human basal ganglia. *J. Neurosci.* **28**, 7143–7152 (2008).
11. A. Mestres-Missé, R. Turner, A. D. Friederici, An anterior-posterior gradient of cognitive control within the dorsomedial striatum. *Neuroimage* **62**, 41–47 (2012).
12. P. Manza, S. Zhang, C.-S. R. Li, H.-C. Leung, Resting-state functional connectivity of the striatum in early-stage Parkinson's disease: Cognitive decline and motor symptomatology. *Hum. Brain Mapp.* **37**, 648–662 (2016).
13. Y. Tian, D. S. Margulies, M. Breakspear, A. Zalesky, Topographic organization of the human subcortex unveiled with functional connectivity gradients. *Nat. Neurosci.* **23**, 1421–1432 (2020).
14. A. J. Peters, J. M. J. Fabre, N. A. Steinmetz, K. D. Harris, M. Carandini, Striatal activity topographically reflects cortical activity. *Nature* **591**, 420–425 (2021).
15. S. J. Kish, K. Shannak, O. Hornykiewicz, Uneven pattern of dopamine loss in the striatum of patients with idiopathic Parkinson's disease. *N. Engl. J. Med.* **318**, 876–880 (1988).
16. R. Moratalla, B. Quinn, L. E. DeLanney, I. Irwin, J. W. Langston, A. M. Graybiel, Differential vulnerability of primate caudate-putamen and striosome-matrix dopamine systems to the neurotoxic effects of 1-methyl-4-phenyl-1,2,3,6-tetrahydropyridine. *Proc. Natl. Acad. Sci. U.S.A.* **89**, 3859–3863 (1992).
17. S. Zaja-Milatovic, D. Milatovic, A. M. Schantz, J. Zhang, K. S. Montine, A. Samii, A. Y. Deutch, T. J. Montine, Dendritic degeneration in neostriatal medium spiny neurons in Parkinson disease. *Neurology* **64**, 545–547 (2005).
18. E. S. Garnett, A. E. Lang, R. Chirakal, G. Firmou, C. Nahmias, A rostrocaudal gradient for aromatic acid decarboxylase in the human striatum. *Can. J. Neurol. Sci.* **14**, 444–447 (1987).
19. M. Politis, Neuroimaging in Parkinson disease: From research setting to clinical practice. *Nat. Rev. Neurol.* **10**, 708–722 (2014).
20. G. N. Stormezand, L. T. Chaves, D. Váñez García, J. Doorduyn, B. M. de Jong, K. L. Leenders, B. P. H. Kremer, R. A. J. O. Dierckx, Intra-striatal gradient analyses of 18F-FDOPA PET scans for differentiation of Parkinsonian disorders. *NeuroImage Clin.* **25**, 102161 (2020).
21. R. Nandhagopal, L. Kuramoto, M. Schulzer, E. Mak, J. Cragg, C. S. Lee, J. McKenzie, S. McCormick, A. Samii, A. Troiano, T. J. Ruth, V. Sossi, R. de la Fuente-Fernandez, D. B. Calne, A. J. Stoessl, Longitudinal progression of sporadic Parkinson's disease: A multi-tracer positron emission tomography study. *Brain* **132**, 2970–2979 (2009).
22. N. I. Bohnen, R. L. Albm, R. A. Koeppe, K. A. Wernette, M. R. Kilbourn, S. Minoshima, K. A. Frey, Positron emission tomography of monoaminergic vesicular binding in aging and Parkinson disease. *J. Cereb. Blood Flow Metab.* **26**, 1198–1212 (2006).
23. G. Tissingh, P. Bergmans, J. Booij, A. Winogrodzka, E. A. van Roeyen, J. C. Stoof, E. C. Wolters, Drug-naïve patients with Parkinson's disease in Hoehn and Yahr stages I and II show a bilateral decrease in striatal dopamine transporters as revealed by [123 I] β -CIT SPECT. *J. Neurol.* **245**, 14–20 (1998).
24. C. G. Goetz, B. C. Tilley, S. R. Shaftman, G. T. Stebbins, S. Fahn, P. Martinez-Martin, W. Poewe, C. Sampaio, M. B. Stern, R. Dodel, B. Dubois, R. Holloway, J. Jankovic, J. Kulisevsky, A. E. Lang, A. Lees, S. Leurgans, P. A. LeWitt, D. Nyenhuis, C. W. Olanow, O. Rascol, A. Schrag, J. A. Teresi, J. J. van Hilten, N. LaPelle; Movement Disorder Society UPDRS Revision Task Force, Movement disorder society-sponsored revision of the unified Parkinson's disease rating scale (MDS-UPDRS): Scale presentation and clinimetric testing results. *Mov. Disord.* **23**, 2129–2170 (2008).
25. N. Weiskopf, S. Mohammadi, A. Lutti, M. F. Callaghan, Advances in MRI-based computational neuroanatomy: From morphometry to in-vivo histology. *Curr. Opin. Neurol.* **28**, 313–322 (2015).
26. K. Yamashita, T. Yoshiura, A. Hiwatashi, T. Noguchi, O. Togao, Y. Takayama, E. Nagao, H. Kamano, M. Hatakenaka, H. Honda, Volumetric asymmetry and differential aging effect of the human caudate nucleus in normal individuals: A prospective MR imaging study. *J. Neuroimaging* **21**, 34–37 (2011).
27. H. Umegaki, G. S. Roth, D. K. Ingram, Aging of the striatum: Mechanisms and interventions. *Age (Dordr.)* **30**, 251–261 (2008).
28. C. Langhammer, N. Krebs, W. Goessler, E. Scheurer, F. Ebner, K. Yen, F. Fazekas, S. Ropele, Quantitative MR imaging of brain iron: A postmortem validation study. *Radiology* **257**, 455–462 (2010).

29. A. Mezer, J. D. Yeatman, N. Stikov, K. N. Kay, N.-J. Cho, R. F. Dougherty, M. L. Perry, J. Parvizi, L. H. Hua, K. Butts-Pauly, B. A. Wandell, Quantifying the local tissue volume and composition in individual brains with magnetic resonance imaging. *Nat. Med.* **19**, 1667–1672 (2013).
30. S. Filo, O. Shtangel, N. Salamon, A. Kol, B. Weisinger, S. Shifman, A. A. Mezer, Disentangling molecular alterations from water-content changes in the aging human brain using quantitative MRI. *Nat. Commun.* **10**, 3403 (2019).
31. N. Weiskopf, M. F. Callaghan, O. Josephs, A. Lutti, S. Mohammadi, Estimating the apparent transverse relaxation time ($R2^*$) from images with different contrasts (ESTATICS) reduces motion artifacts. *Front. Neurosci.* **8**, 278 (2014).
32. Z. Shams, D. G. Norris, J. P. Marques, A comparison of in vivo MRI based cortical myelin mapping using T1w/T2w and R1 mapping at 3 T. *PLOS ONE* **14**, e0218089 (2019).
33. M. F. Glasser, D. C. Van Essen, Mapping human cortical areas in vivo based on myelin content as revealed by T1- and T2-weighted MRI. *J. Neurosci.* **31**, 11597–11616 (2011).
34. D. S. Margulies, S. S. Ghosh, A. Goulas, M. Falkiewicz, J. M. Huentenburger, G. Langs, G. Bezgin, S. B. Eickhoff, F. X. Castellanos, M. Petrides, E. Jefferies, J. Smallwood, Situating the default-mode network along a principal gradient of macroscale cortical organization. *Proc. Natl. Acad. Sci. U.S.A.* **113**, 12574–12579 (2016).
35. R. Schurr, Y. Duan, A. M. Norcia, S. Ogawa, J. D. Yeatman, A. A. Mezer, Tractography optimization using quantitative T1 mapping in the human optic radiation. *Neuroimage* **181**, 645–658 (2018).
36. D. C. Van Essen, S. M. Smith, D. M. Barch, T. E. J. Behrens, E. Yacoub, K. Ugurbil; WU-Minn HCP Consortium, The WU-Minn human connectome project: An overview. *Neuroimage* **80**, 62–79 (2013).
37. A. Brück, S. Aalto, E. Rauhalu, J. Bergman, R. Marttila, J. O. Rinne, A follow-up study on $6\text{-}^{18}\text{F}$ fluoro-L-dopa uptake in early Parkinson's disease shows nonlinear progression in the putamen. *Mov. Disord.* **24**, 1009–1015 (2009).
38. E. J. Modestino, C. Amenechi, A. M. Reinhofer, P. O'Toole, Side-of-onset of Parkinson's disease in relation to neuropsychological measures. *Brain Behav.* **7**, e00590 (2017).
39. P. S. Foster, R. C. Yung, V. Drago, G. P. Crucian, K. M. Heilman, Working memory in Parkinson's disease: The effects of depression and side of onset of motor symptoms. *Neuropsychology* **27**, 303–313 (2013).
40. F. A. Middleton, P. L. Strick, Basal ganglia and cerebellar loops: Motor and cognitive circuits. *Brain Res. Rev.* **31**, 236–250 (2000).
41. G. E. Alexander, M. R. DeLong, P. L. Strick, Parallel organization of functionally segregated circuits linking basal ganglia and cortex. *Annu. Rev. Neurosci.* **9**, 357–381 (1986).
42. A. Mechelli, K. J. Friston, R. S. Frackowiak, C. J. Price, Structural covariance in the human cortex. *J. Neurosci.* **25**, 8303–8310 (2005).
43. A. Alexander-Bloch, J. N. Giedd, E. Bullmore, Imaging structural co-variance between human brain regions. *Nat. Rev. Neurosci.* **14**, 322–336 (2013).
44. K. Hagimoto, S. Takami, F. Murakami, Y. Tanabe, Distinct migratory behaviors of striosomes and matrix cells underlying the mosaic formation in the developing striatum. *J. Comp. Neurol.* **525**, 794–817 (2017).
45. A. F. Marquand, K. V. Haak, C. F. Beckmann, Functional corticostriatal connection topographies predict goal-directed behaviour in humans. *Nat. Hum. Behav.* **1**, 0146 (2017).
46. J. F. O'Rawe, J. S. Ide, H.-C. Leung, Model testing for distinctive functional connectivity gradients with resting-state fMRI data. *Neuroimage* **185**, 102–110 (2019).
47. J. Sedlacik, K. Boelmans, U. Löbel, B. Holst, S. Siemonsen, J. Fiehler, Reversible, irreversible and effective transverse relaxation rates in normal aging brain at 3 T. *Neuroimage* **84**, 1032–1041 (2014).
48. A. De Barros, G. Arribat, J. A. Lotterie, G. Dominguez, P. Chaynes, P. Péran, Iron distribution in the lentiform nucleus: A post-mortem MRI and histology study. *Brain Struct. Funct.* **226**, 351–364 (2021).
49. M. F. Callaghan, G. Helms, A. Lutti, S. Mohammadi, N. Weiskopf, A general linear relaxation model of R1 using imaging data. *Magn. Reson. Med.* **73**, 1309–1314 (2015).
50. C. Laule, I. M. Vavasour, S. H. Kolind, D. K. B. Li, T. L. Trabulsee, G. R. W. Moore, A. L. MacKay, Magnetic resonance imaging of myelin. *Neurotherapeutics* **4**, 460–484 (2007).
51. J. A. Pineda-Pardo, A. Sánchez-Ferro, M. H. G. Monje, N. Pavese, J. A. Obeso, Onset pattern of nigrostriatal denervation in early Parkinson's disease. *Brain* **1018–1028** (2022).
52. R. A. McCutcheon, A. Abi-Dargham, O. D. Howes, Schizophrenia, dopamine and the Striatum: From biology to symptoms. *Trends Neurosci.* **42**, 205–220 (2019).
53. T. Xu, K. H. Nanning, E. Schwartz, S. J. Hong, J. T. Vogelstein, A. Goulas, D. A. Fair, C. E. Schroeder, D. S. Margulies, J. Smallwood, M. P. Milham, G. Langs, Cross-species functional alignment reveals evolutionary hierarchy within the connectome. *Neuroimage* **223**, 117346 (2020).
54. J. M. Huentenburger, P. L. Bazin, D. S. Margulies, Large-scale gradients in human cortical organization. *Trends Cogn. Sci.* **22**, 21–31 (2018).
55. S. Berman, R. Schurr, G. Atlan, A. Citri, A. A. Mezer, Automatic segmentation of the dorsal claustrum in humans using in vivo high-resolution MRI. *Cereb. Cortex Commun.* **1**, 1–14 (2020).
56. C. Paquola, R. Vos de Wael, K. Wagstly, R. A. I. Bethlehem, S. J. Hong, J. Seidlitz, E. T. Bullmore, A. C. Evans, B. Misis, D. S. Margulies, J. Smallwood, B. C. Bernhardt, Microstructural and functional gradients are increasingly dissociated in transmodal cortices. *PLOS Biol.* **17**, e3000284 (2019).
57. S. Larivière, R. Vos de Wael, S. J. Hong, C. Paquola, S. Tavakol, A. J. Lowe, D. V. Schrader, B. C. Bernhardt, Multiscale structure-function gradients in the neonatal connectome. *Cereb. Cortex* **30**, 47–58 (2020).
58. S. N. Haber, K. S. Kim, P. Mally, R. Calzavara, Reward-related cortical inputs define a large striatal region in primates that interface with associative cortical connections, providing a substrate for incentive-based learning. *J. Neurosci.* **26**, 8368–8376 (2006).
59. X. Liu, S. B. Eickhoff, F. Hoffstaedter, S. Genon, S. Caspers, K. Reetz, I. Dogan, C. R. Eickhoff, J. Chen, J. Caspers, N. Reuter, C. Mathys, A. Aleman, R. Jardi, V. Riedl, I. E. Sommer, K. R. Patil, Joint multi-modal parcellation of the human striatum: Functions and clinical relevance. *Neurosci. Bull.* **36**, 1123–1136 (2020).
60. J. D. Yeatman, R. F. Dougherty, N. J. Myall, B. A. Wandell, H. M. Feldman, Tract profiles of white matter properties: Automating fiber-tract quantification. *PLOS ONE* **7**, e49790 (2012).
61. M. Fukunaga, T. Q. Li, P. van Gelderen, J. A. de Zwart, K. Shmueli, B. Yao, J. Lee, D. Maric, M. A. Aronova, G. Zhang, R. D. Leapman, J. F. Schenck, H. Merkle, J. H. Duyn, Layer-specific variation of iron content in cerebral cortex as a source of MRI contrast. *Proc. Natl. Acad. Sci. U.S.A.* **107**, 3834–3839 (2010).
62. M. D. Waehnert, J. Dinse, M. Weiss, M. N. Streicher, P. Waehnert, S. Geyer, R. Turner, P. L. Bazin, Anatomically motivated modeling of cortical laminae. *Neuroimage* **93**, 210–220 (2014).
63. P. McColgan, J. Joubert, S. J. Tabrizi, G. Rees, The human motor cortex microcircuit: Insights for neurodegenerative disease. *Nat. Rev. Neurosci.* **21**, 401–415 (2020).
64. G. Blazquez Freches, K. V. Haak, C. F. Beckmann, R. B. Mars, Connectivity gradients on tractography data: Pipeline and example applications. *Hum. Brain Mapp.* **42**, 5827–5845 (2021).
65. L. G. Astrakas, M. I. Argyropoulou, Shifting from region of interest (ROI) to voxel-based analysis in human brain mapping. *Pediatr. Radiol.* **40**, 1857–1867 (2010).
66. K. Hua, J. Zhang, S. Wakana, H. Jiang, X. Li, D. S. Reich, P. A. Calabresi, J. J. Pekar, P. C. M. van Zijl, S. Mori, Tract probability maps in stereotaxic spaces: Analyses of white matter anatomy and tract-specific quantification. *Neuroimage* **39**, 336–347 (2008).
67. N. Weiskopf, J. Suckling, G. Williams, M. M. Correia, B. Inkster, R. Tait, C. Ooi, E. T. Bullmore, A. Lutti, Quantitative multi-parameter mapping of R1, PD*, MT, and R2* at 3 T: A multi-center validation. *Front. Neurosci.* **7**, 95 (2013).
68. B. Patenaude, S. M. Smith, D. N. Kennedy, M. Jenkinson, A Bayesian model of shape and appearance for subcortical brain segmentation. *Neuroimage* **56**, 907–922 (2011).
69. J. Yeatman, B. Wandell, A. Mezer, Lifespan maturation and degeneration of human brain white matter. *Nat. Commun.* **5**, 4932 (2014).
70. A. Alkemade, M. J. Mulder, J. M. Groot, B. R. Isaacs, N. van Berendonk, N. Lute, S. J. S. Isherwood, P. L. Bazin, B. U. Forstmann, The Amsterdam Ultra-high field adult lifespan database (AHEAD): A freely available multimodal 7 Tesla submillimeter magnetic resonance imaging database. *Neuroimage* **221**, 117200 (2020).
71. B. Fischl, FreeSurfer. *Neuroimage* **62**, 774–781 (2012).
72. R. S. Desikan, F. Ségonne, B. Fischl, B. T. Quinn, B. C. Dickerson, D. Blacker, R. L. Buckner, A. M. Dale, R. P. Maguire, B. T. Hyman, M. S. Albert, R. J. Killiany, An automated labeling system for subdividing the human cerebral cortex on MRI scans into gyral based regions of interest. *Neuroimage* **31**, 968–980 (2006).
73. Y. Benjamini, Y. Hochberg, Controlling the false discovery rate: A practical and powerful approach to multiple testing. *J. R. Stat. Soc. Ser. B* **57**, 289–300 (1995).
74. M. F. Glasser, S. N. Sotiropoulos, J. A. Wilson, T. S. Coalson, B. Fischl, J. L. Andersson, J. Xu, S. Jbabdi, M. Webster, J. R. Polimeni, D. Van Essen, M. Jenkinson; WU-Minn HCP Consortium, The minimal preprocessing pipelines for the human connectome project. *Neuroimage* **80**, 105–124 (2013).
75. E. Drori, A. Mezer, mrGrad, version 1.0, Zenodo (2022); <https://doi.org/10.5281/zenodo.5920358>.
76. A. Mezer, A. Rokem, S. Berman, T. Hastie, B. A. Wandell, Evaluating quantitative proton-density-mapping methods. *Hum. Brain Mapp.* **37**, 3623–3635 (2016).

Acknowledgments: We thank H. Bergman, D. Arkadir, G. Yahalom, K. MacNiven, R. Schurr, and S. Filo for their critical reading of the manuscript and their very useful comments. **Funding:** This research was supported by the Israel Science Foundation (grant 1169/20) given to A.A.M. **Author contributions:** Conceptualization, methodology, and writing: E.D. and A.A.M. Analysis and visualization: E.D. and S.B. Supervision: A.A.M. **Competing interests:** PCT Patent Application No. PCT/IL2021/050762 "Measuring biological gradients along the human dorsal

striatum in vivo using quantitative MRI" has been filed by the Hebrew University of Jerusalem on 22 June 2021. The authors declare no other competing interests. **Data and materials availability:** All data needed to evaluate the conclusions in the paper are present in the paper and/or the Supplementary Materials. The MATLAB implementation of our tool for computation of qMRI gradients along anatomical axes of subcortical structures is available on GitHub at <https://github.com/MezerLab/mrGrad>, and on Zenodo (75) at <https://zenodo.org/record/5920358>. Datasets A and B can be provided by A.A.M. pending scientific review and a

completed material transfer agreement. Requests for datasets A and B should be submitted to aviv.mezer@mail.huji.ac.il.

Submitted 1 September 2021

Accepted 2 June 2022

Published 15 July 2022

10.1126/sciadv.abm1971